# Subtropical and Extratropical South American Intraseasonal Variability: A Normal-Mode Approach

**Victor C. Mayta[1,2*], André Seiji Wakate Teruya [3], Breno Raphaldini [4], Pedro L. Silva Dias [3], and Camila Sapucci [3].**

[1]Department of Climate and Space Science and Engineering, University of Michigan, Ann Arbor, Michigan
[2]Department of Atmospheric and Oceanic Sciences, University of Wisconsin, Madison, Wisconsin
[3]Departamento de Ciências Atmosféricas, IAG, Universidade de São Paulo, São Paulo, SP, Brasil
[4]Department of Mathematical Sciences, Durham University, Stockton Road Durham-UK DH1 3LE

**Key Points:**

- Extratropical Rossby waves play an important role in the South American intraseasonal rainfall variability, mainly during the dry season
- Normal-mode decomposition of the South American intraseasonal variability shows that the dipole SESA-SACZ pattern is dominated by rotational modes
- The normal-mode decomposition provides a powerful tool for diagnosing circulation model issues in order to improve rainfall prediction

*Climate and Space Research Building University of Michigan, 2455 Hayward St., Ann Arbor.

Corresponding author: Victor C. Mayta, vmayta@umich.edu

## Abstract

Instead of using the traditional space-time Fourier analysis of filtered specific atmospheric fields, a normal-mode decomposition method is used to analyze the South American intraseasonal variability. Intraseasonal variability was separate into the 30-90-day Low-Frequency Intraseasonal (LFI) and 10-30-day High-Frequency Intraseasonal (HFI) variability, and analyzed the contribution of the rotational (ROT) and inertio-gravity (IGW) components to the observed convective and circulation features. The seasonal cycle of the LFI and HFI convective and dynamical structure is well-described by the first leading pattern (EOF1). The LFI EOF1 spatial structure during the rainy season is the dipole-like between the South Atlantic Convergence Zone (SACZ) and southeastern South America (SESA), influenced by the large-scale Madden-Julian Oscillation (MJO). During the dry season, alternating periods of enhanced and suppressed convection over South America are primarily controlled by extratropical wave disturbances. The HFI spatial pattern also resembles the SESA–SACZ structure, in response to the Rossby wave trains. Results based on normal-mode decomposition of reanalysis data and the LFI and HFI indices show that the tropospheric circulation and SESA–SACZ convective structure observed over South America are dominated by ROT modes (e.g., Rossby). A considerable portion of the LFI variability is also associated with the inertio-gravity (IGW) modes (e.g., Kelvin mode), prevailing mainly during the rainy season. The proposed decomposition methodology provides new insights into the dynamics of the South American intraseasonal variability, giving a powerful tool for diagnosing circulation model issues in order to improve the prediction of precipitation.



## Plain Language Summary

In this study, we proposed a decomposition methodology of the dynamic of the South American intraseasonal variability, giving a powerful tool for diagnosing circulation model issues in order to improve the prediction of precipitation. We find that intraseasonal variability circulation and the corresponding SESA–SACZ convective structure observed over South America are dominated by rotational modes (Rossby and mixed waves). Our results also show that tropical convection, linked with the large-scale Madden-Julian Oscillation, in many instances triggers midlatitude Rossby wave trains.


## 1 Introduction

A substantial fraction of the submonthly to intraseasonal-scale convective variability over South America is associated with the large-scale subtropical extratropical atmospheric disturbances (Satyamurty et al., 1998; Liebmann et al., 1999; Paegle et al., 2000; Jones & Carvalho, 2002; Liebmann et al., 2011; C. S. Vera et al., 2018; Gelbrecht et al., 2018); among others. In fact, one of the most distinctive features which characterize the South America wet season (October-April) is the presence of the South Atlantic Convergence Zone (SACZ). The SACZ varies on many time-scales and its activity is largely modulated by transient disturbances (Nogués-Paegle & Mo, 1997; Liebmann et al., 1999; Cunningham & Cavalcanti, 2006). Rossby wave trains, which can be forced by the tropical convective activity such as the Madden-Julian oscillation (MJO), induce intraseasonal variability over South America (Gonzalez & Vera, 2014; C. S. Vera et al., 2018; Adames & Wallace, 2014). This interaction between tropics and extratropics is frequently linked to the development of the Pacific-South America (PSA) teleconnection pattern (e.g., (Mo & Higgins, 1998)). The existence of these disturbances was well-documented by (Liebmann et al., 1999) using 2-30-day filtered OLR anomalies. They found two preferred paths of Rossby wave train patterns in the Southern Hemisphere: one affecting the SACZ and another influencing the southwestern Amazon. In fact, the southern Amazon pattern resembles the “cold surges” phenomenon discussed in detail by (Garreaud & Wallace, 1998), (Garreaud, 2000), (Lupo et al., 2001), among others. In addition, these

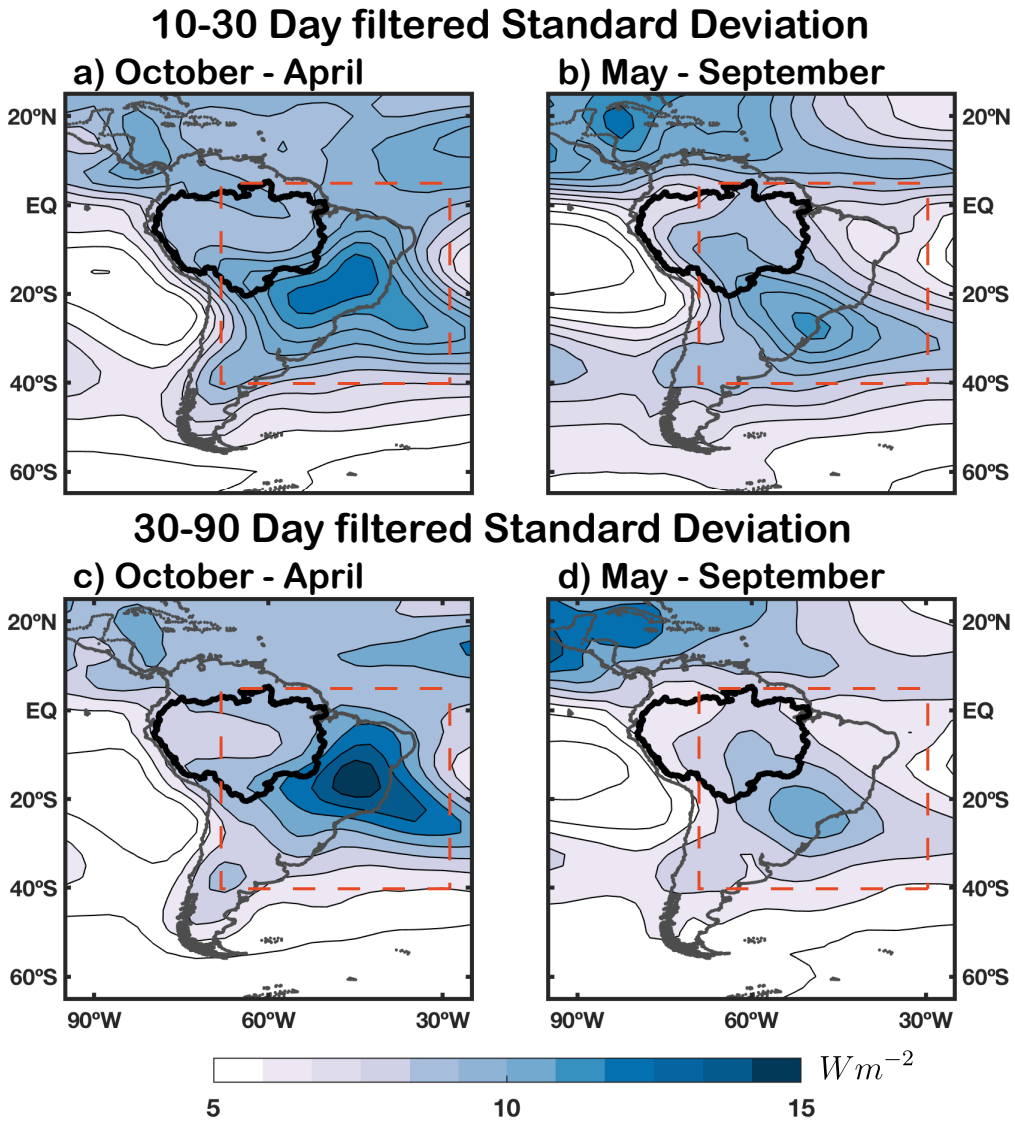


**Figure 1.** (Top) Standard deviation of daily 10-30-day-filtered OLR in $Wm^{-2}$ for the (a) October-April, and (b) May-September period. (Bottom) As in the top row, but showing standard deviation of daily 30-90-day-filtered OLR. Shading interval are shown by the legend.

Rossby waveguides represent one of the preferred propagation routes in South America (Grimm & Silva Dias, 1995; Ambrizzi & Hoskins, 1997).

Recently, a new approach to study the intraseasonal variability over South America was introduced based on separating the classical intraseasonal variability into 10-30-day high-frequency intraseasonal variability and the 30-90-day low-frequency intraseasonal variability (Gonzalez & Vera, 2014; C. S. Vera et al., 2018). Early studies such as (Liebmann et al., 1999) have already documented spectral peaks at 50 days period over the SACZ and the Amazon (corresponding to the canonical MJO effect), and other peaks near 27, 16, 10, and 8 days. Similar spectral peaks were detected on observed rainfall data over the Amazon (Mayta et al., 2020). As documented by the previous references, regions located on the equatorial domain (e.g, Northeast of Brazil) also show clear spec-

tral peaks centered around 48 days. It is widely documented that the most distinctive pattern of the 30-90-days intraseasonal variability over South America, during austral summer (corresponding to the wet season), is the dipole-like configuration between southeastern South America (SESA) and the SACZ (Casarin & Kousky, 1986; Nogués-Paegle & Mo, 1997; Souza & Ambrizzi, 2006; C. Vera et al., 2006; C. S. Vera et al., 2018; Alvarez et al., 2017; Gelbrecht et al., 2018). In addition, recent studies demonstrated that the MJO activity is noticeable year-round over South America (Alvarez et al., 2016; C. S. Vera et al., 2018), which includes the Amazon region (Mayta et al., 2019). During the dry season (June to August), the convective features are slightly different from the wet season. Both enhanced and suppressed convection cover a broad South America region (see Fig. 5 in (C. S. Vera et al., 2018)). On the other hand, on the 10-30-day HFI variability over South America, the dipole-like structure (SESA-SACZ) is still visible, with a stronger signal over the SESA region during the dry season (Gonzalez & Vera, 2014; C. S. Vera et al., 2018).

The low-frequency intraseasonal rainfall variability over South America, on the other hand, is not strictly associated with the forcing produced by the equatorially propagating MJO events. There are other mechanisms (e.g., through Southern Hemisphere Rossby wave trains) playing an important role in the modulation of high-frequency convective activity (Grimm & Silva Dias, 1995; Ambrizzi & Hoskins, 1997; Liebmann et al., 1999; Gonzalez & Vera, 2014; C. S. Vera et al., 2018; Grimm, 2019). Recently, (Mayta et al., 2019) found that on average 35% of the intraseasonal rainfall events over the Amazon (which extends from 5° to 20°) do not have the MJO as a precursor. In addition, (C. S. Vera et al., 2018) documented similar spatial patterns over South America (SESA-SACZ dipole-like), in both low- and high-frequency intraseasonal variability. These results raised some questions, for instance: which mechanisms are responsible for this configuration in the intraseasonal time-scales? (C. F. M. Raupp & Silva Dias, 2009; C. Raupp & Silva Dias, 2010) and (Ramirez et al., 2017) discussed the possibility of a nonlinear process leading to internal variability on the intraseasonal band through the nonlinear resonance of equatorial waves, associated with convective forcing, linking the diurnal variability to the modulation of the intraseasonal variability.

On the other hand, low-frequency intraseasonal precipitation over different South American regions is frequently analyzed using different MJO indices. However, most of these indices do not properly represent the complex eastward MJO propagation over tropical regions, mainly during the austral winter (Kikuchi et al., 2012; Wang et al., 2018), and over South America poorly represent its modulation in precipitation (Mayta et al., 2020). In addition, the South America intraseasonal variability is always described based on directly observed data (e.g., outgoing long-wave radiation, precipitation) and using the traditional principal component analysis. However, complex interaction in intraseasonal time-scales and shorter, indeed, need a more complex approach. In this line, (Gelbrecht et al., 2018) using phase synchronization technique demonstrated that the SESA–SACZ dipole-like precipitation structure is caused mainly by the extratropical Rossby waves. However, some limiting factors of their approach include the irregular/intermittent character of the phenomena often misrepresented by linear techniques such as EOF, as well as the lack of detailed attribution of types and wave-numbers of the modes associated with the SESA–SACZ variability. The first drawback can be overcome by using more intrinsically nonlinear approaches like the self-organizing maps (SOM, (Chu et al., 2017)) than a traditional linear technique such as EOFs. The second problem can be addressed by using the so-called normal mode functions (NMF), which are orthogonal eigenfunctions of the linearized primitive equations on a sphere (Kasahara & Puri, 1981; Tanaka, 1985). Indeed, recent works used NMF to characterize physical properties representative of the MJO (Žagar & Franzke, 2015; Kitsios et al., 2019), and other tropical atmospheric disturbances (Castanheira & Marques, 2015; Raphaldini et al., 2020). An earlier study (Baer, 1972) suggested a two-dimensional index ($index = s + n$) as a measure of horizontal scale as in (Kasahara, 1980) (see his Fig. 5). Where $s$ and $n$ are the

zonal wavenumbers and meridional indices, respectively. Thus, in this study we will project 3D atmospheric fields onto normal modes of the global primitive equations, based on the Kasahara and Puri, 1981 approach, to determine the modes that more closely describe the observations.

Several key research issues relevant to intraseasonal oscillation over South America, which were not explored in previous studies, will be addressed in the present study. Therefore, the main goal of this study is to further explore the high- and low-frequency intraseasonal rainfall variability over South America.

- Describe the seasonal cycle of intraseasonal variability in South America and its relationship with both circulation anomalies and tropical convection.

First, through the leading EOFs, explore how the low-frequency intraseasonal is influenced by the high-frequency intraseasonal variability band.

- Present a multivariate three-dimensional analysis of the intraseasonal circulation based on normal mode expansion.

Thus, and to assess the physical mechanism associated with the 30-90-day Low-frequency (hereafter LFI), and the 10-30-day High-frequency (hereafter HFI) we computed a decomposition of both frequencies band in terms of normal-mode functions by performing linear regressions between the indices and normal-mode amplitudes. The normal-mode functions constitute a complete basis for the atmospheric circulation, i.e., atmospheric wind and pressure (Kasahara & Puri, 1981). Therefore, this procedure will provide the most relevant modes contributing to the presence of the SESA–SACZ dipole configuration on 30-90-day LFI, as well as the modes associated with the extratropical Rossby wave trains.

The paper is organized as follows. Section 2 presents a brief description of the data and methodologies. In section 3, we described the seasonal cycle of LFI and HFI variability, including their dynamical mechanisms in section 4. The relationship between the LFI and HFI is discussed in section 4.3. Sections 5 and 6 analyze the normal-mode components related to the LFI and HFI variability over South America. Finally, the main results are summarized and discussed in section 7.

## 2 Data and Methodology

### 2.1 Data

Satellite-observed outgoing longwave radiation (OLR) data are used as a proxy for the large-scale convection over South America. The OLR data was obtained from the National Oceanic and Atmospheric Administration - NOAA (Liebmann & Smith, 1996). Figure 1 shows the geographical standard deviation distribution of the LFI and HFI filtered OLR over 1980-2016 and considering the South American Monsoon System (SAMS) period (October-April, hereafter wet season) and the absence of SAMS (May-September, hereafter dry season) period. Over South America, during the Oct-Apr period, both LFI and HFI show peak activity over the mean position of the SACZ (Figures 1a, c). This signal extends toward the South Atlantic Ocean and southeastern Amazon. Similar variance was documented by (Liebmann et al., 1999) during austral summer (see their Fig. 3a). On the other hand, the LFI and HFI convective activity during the austral dry period (May-Sep) peak over SESA. Areas with large standard deviation values in HFI extend towards the north, covering almost the entire Amazon (Fig. 1b).

We make use of daily data from the fifth reanalysis from the European Centre for Medium-Range Weather Forecasts (ECMWF) (ERA5; (Hersbach et al., 2019)). The date

covers the time period starting in 1979 and ending in 2019. The dataset has a horizontal spectral resolution of N80 (approximately $1.125° \times 1.125°$) and 137 vertical levels ranging from 1012.04 up to 0.01 hPa. The variables used in this study are geopotential height ($z$), temperature ($T$), horizontal winds ($u$, $v$), specific humidity ($q$), and surface pressure ($sp$).

### 2.2 Filtering and empirical orthogonal function (EOF) Technique

Daily anomalies of the convection and dynamical fields are calculated at each grid point by subtracting the first three harmonics (i.e., the annual cycle and 2 subsequent harmonics) of the entire 37-years time-series in order to remove the seasonal cycle. The LFI and HFI filtered anomalies are obtained by applying Fast Fourier Transform (FFT), considering a frequency domain of 30-90-days and 10-30 days, respectively. Filtered OLR within the South America domain (red box in Fig. 1) is then submitted to a covariance matrix EOF analysis that retains the local variance of the EOF fluctuations. As in (Kiladis et al., 2014), EOFs are computed considering the entire record (from 1979-2016) but centered on each day of the calendar year using a sliding window. A 121-days and 61-days window lengths are considered for the LFI and HFI, respectively. This approach takes into account for the complex convective propagation over the region and better characterizes the seasonal variation of the intraseasonal variability. The first principal component (PC1) time series of the EOF is used to compute regression analysis and to define LFI and HFI events. In addition, the leading EOF time series is used in the decomposition of the LFI and HFI in terms of the normal-mode functions.

### 2.3 Defining the intraseasonal index and events

Considering that the first mode is the dominant mode in the low and high-frequency intraseasonal variability, we use the PC1 time series to define the corresponding index and identify events. Thus, the PC1 time series of the 30-90 day EOF1 is referred hereafter as the LFI index. Similarly, the PC1 time series of the 10-30 day EOF1 is referred as the HFI index. In addition, using similar criteria proposed by (Mayta et al., 2019), LFI events over South America are defined considering the corresponding PC1 time series. According to this criterion, the 30-90-day PC1 time series, during the event, must be lower than -1.0 standard deviation. The minimum duration of the event must be 5 days (like a single MJO index phase average duration). To verify that a singular LFI event is preceded by a large-scale MJO active phase propagating into the South America region, two widely-used existing MJO indices are considered: (1) OLR-based MJO (OMI index; (Kiladis et al., 2014)); and (2) combined convectively- and dynamically-based MJO (RMM index; (M. C. Wheeler & Hendon, 2004)). Finally, the occurrence of each LFI event is attributed to the associated precursor. We divided all precursors into three main types: (1) tropical precursors (T) when a LFI event is preceded by the MJO eastward-propagation; (2) extratropical precursor (E) associated with the extratropical Rossby wave trains; and (3) other precursors (OP) means that LFI events do not have precursors of either type 1 or 2 above.

### 2.4 Linear regression

The LFI and HFI circulation and convection structure presented in this study are based on linear regression. We regress the standardized PC1 30–90 and PC1 10-30 against dynamical and convective fields (OLR, velocity potential, streamfunction, and winds at 200-hPa). When each PC1 reaches its lowest value is defined as day 0. The statistical significance of these results is assessed based on the two-tailed Student's t-test. This method takes into account the correlation coefficients and an effective number of independent samples (degrees of freedom) based on the decorrelation time-scale, as in (Livezey & Chen, 1983) (more details in (Kiladis & Weickmann, 1992) and (Mayta et al., 2021)). Two sub-

seasons are considered for the analysis: October-April, the period of active SAMS season, and May-September as the period of the non-monsoon season.

### 2.5 Global Normal-Mode Function (NMF) Expansion

Given that the reanalysis data are provided for the entire globe, it is desirable to associate them with normal modes of the equations on the sphere. The linearized system of the atmospheric primitive equation in sigma coordinates and the vertical direction is given by,

$$\frac{\partial u}{\partial t} - 2\Omega v \sin(\phi) = -\frac{g}{a\cos(\phi)}\frac{\partial h}{\partial \lambda}, \tag{1}$$

$$\frac{\partial v}{\partial t} + 2\Omega u \sin(\phi) = -\frac{g}{a}\frac{\partial h}{\partial \phi}, \tag{2}$$

$$\frac{\partial}{\partial t}\Big[\frac{\partial}{\partial \sigma}\Big(\frac{g\sigma}{R\Gamma_0}\frac{\partial h}{\partial \sigma}\Big)\Big] - \nabla \cdot \mathbf{V} = 0, \tag{3}$$

where $\mathbf{V} = (u, v)$ is the velocity field given by its zonal and meridional components, $\Omega$ is the Earth's rotation rate and $a$ its radius. $h = P/g$ represents the modified geopotential height, with $P$ the pressure field and $g$ the acceleration of gravity. $\Gamma_0 = \kappa T_0/\sigma - dT_0/d\sigma$ is the static stability parameter, where $T_0 = T_0(\sigma)$ is the globally horizontally averaged temperature. The boundary conditions are no-penetration conditions at the top and at the bottom ($\sigma = \sigma_T$ and $\sigma = 1$).

The solutions of this coupled system are obtained by performing a separation of variables into a horizontal and a vertical structure:

$$\begin{bmatrix} u'(\lambda,\phi,\sigma,t) \\ v'(\lambda,\phi,\sigma,t) \\ h'(\lambda,\phi,\sigma,t) \end{bmatrix} = G(\sigma) \begin{bmatrix} u(\lambda,\phi,t) \\ v(\lambda,\phi,t) \\ h(\lambda,\phi,t) \end{bmatrix}, \tag{4}$$

where the vertical structure function is given by $G(\sigma)$ and is expanded in terms of a basis of orthonormal basis functions:

$$G(\sigma) = \sum_{m=1}^{M} c_m G_m(\sigma), \tag{5}$$

where $G_m(\sigma)$ are the eigenfunctions of the vertical structure eigenproblem such that,

$$\int_{\sigma_T}^{1} G_m(\sigma) G_n(\sigma) d\sigma = \delta_{mn}, \tag{6}$$

where $\delta_{mn}$ is the Kronecker delta, that is equal to 1 if $m = n$, and equal to 0 otherwise. And the coefficient $c_m$ is calculated by

$$c_m = \int_{\sigma_T}^{1} G(\sigma) G_m(\sigma) d\sigma, \tag{7}$$

$\sigma_T$ is model top in $\sigma$-coordinate. The horizontal structure-function is given by the product of an oscillatory term in time and a spatial structure as follow,

$$\mathbf{U}(\lambda,\phi,t) = \sum_{n=0}^{N}\sum_{k=0}^{K} \mathbf{H}_n^k(\lambda,\phi) e^{(-i\omega_n^k t)}, \tag{8}$$

where $n$ and $k$ are the meridional and the zonal mode indices, respectively. The spatial structure $\mathbf{H}_n^k$ is described by Hough modes. Given a vector field $\mathbf{X}$, on a discrete grid over the sphere, the projection of $\mathbf{X}$ onto the basis of normal mode function is obtained by using the inner product from the vertical eigenvalue problem:

$$\mathbf{X}(\lambda,\phi,\sigma_j) = \sum_{m=1}^{M} \mathbf{X}_m(\lambda,\phi) G_m(\sigma_j), \tag{9}$$

providing a set of horizontal structures $\mathbf{X}_m$, for each vertical level $j = 1, ..., J$, and $G_m(\sigma_j)$ is a discretized version of the vertical structure function $G_m(\sigma)$ via finite differences. $\mathbf{X}_m$ is then projected onto the basis of Hough functions to obtain the normal mode coefficient associated with indices $(m, n, k)$:

$$\chi_{mnk} = \int_0^{2\pi}\int_{-\pi/2}^{\pi/2} \mathbf{X}_m \cdot \left[\mathbf{H}_n^k\right]^* \sin(\phi) d\phi d\lambda. \tag{10}$$

Based on this, the vector field $\mathbf{X}$ is expressed as a sum of components corresponding to each of the elements of the basis of the normal mode functions with their respective amplitude and the index $^*$ represents the complex conjugate of the Hough mode:

$$\mathbf{X}(\lambda,\phi,\sigma_j) = \sum_{m=1}^{M}\sum_{n=0}^{N}\sum_{k=0}^{K} \chi_{kmn} G_m(\sigma_j) \mathbf{H}_n^k(\lambda,\phi). \tag{11}$$

In this study, we use the open-source software MODES (Žagar et al., 2015) that performs these operations given the ERA5 reanalysis. In other words, given a set of observed (reanalysis) horizontal winds and modified geopotential height fields[1] evolving in time $\mathbf{W} = (u(\lambda,\phi,\sigma,t), v(\lambda,\phi,\sigma,t), h(\lambda,\phi,\sigma,t))^T$. We use the discretized inner product (replacing the integrals by summations over the grid points) defined by the combination of Eq. (10) and Eq. (7) to project the observed field onto the basis of normal mode functions. This provides a unique decomposition of the observed fields. Thus, the amplitude $\chi_{mnk}$ of the mode with zonal wavenumber $k$, meridional index $n$ and vertical index $m$ associated with $\mathbf{W}$ at time $t$ is given by,

$$\chi_{mnk}(t) = \langle \mathbf{W}(\lambda,\phi,\sigma,t), \mathbf{N}_{mnk}(\lambda,\phi,\sigma)\rangle \tag{12a}$$

$$= \int_{\sigma_T}^{1}\int_0^{2\pi}\int_{-\pi/2}^{\pi/2} \mathbf{W}(\lambda,\phi,\sigma,t) \cdot \left[\mathbf{H}_n^k(\lambda,\phi) G_m(\sigma)\right]^* \sin(\phi) d\phi d\lambda d\sigma \tag{12b}$$

where the normal mode function $\mathbf{N}_{mnk}$ is the product of the vertical structure function $G_m(\sigma)$ by the horizontal structure function $\mathbf{H}_n^k(\lambda,\phi)$.

One of the main advantages of this approach is to attribute systematically a certain type of atmospheric waves (i.e., Rossby, inertio-gravity, Kelvin, mixed Rossby-gravity)

[1] The modified geopotential height is derived from the air temperature, surface pressure, specific humidity, and geopotential height fields.

to observed fields. In this scenario, the role of nonlinear terms and the momentum and energy sources/sinks are included in the phase space-time evolution equation given by

$$\frac{d\chi_{mnk}}{dt} - i\omega\chi_{mnk} = \eta_{mnk} + f_{mnk} \tag{13}$$

where $\eta_{mnk} + f_{mnk}$ represent the projection on the nonlinear terms and forcing terms in physical space on the normal mode $\chi_{mnk}$. Thus, the amplitude and phase of a particular normal mode (such as a Kelvin wave with the vertical structure given by $G_m(\sigma)$ with meridional mode $n$ and zonal wavenumber $k$ changes in time according to the impact of the combined effect of the nonlinearities and the physical forcing. $\eta_{mnk}$ represents the role in the interaction of all possible modes onto $\chi_{mnk}$. Thus, in the absence of nonlinearities and forcing, the particular mode represented by the Kelvin wave should maintain its amplitude and the non-dispersive phase speed is the theoretical value which is approximately $\sqrt{gh_m}$, where $h_m$ is the eigenvalue of the vertical structure equation. Thus, Eq. (13) shows that any deviation of the linear theoretical phase speed can only be attributed to the role of the nonlinearity and forcing. In a linearized state about a climatological zonal flow, the effect is included in both $\eta_{mnk}$ and $f_{mnk}$ if the basic state is not constant. The forcing term projection is required in order to have a stationary basic state.

In the usual interpretation of the Wheeler-Kiladis diagram (M. Wheeler & Kiladis, 1999), the reference Matsuno dispersion relation is provided in the background for a particular vertical mode with equivalent depth that more closely represents the influence of deep tropospheric diabatic convective heating ( $\sqrt{gh_m} \cong 30ms^{-1}$). Therefore, when spectral energy is found along with the theoretical Kelvin regime, it means that free Kelvin waves contain a substantial amount of spectral power. However, the role of nonlinearities and forcing may distort the linear propagation speed (eventually inverting the direction) and cause substantial time change in the evolution of the Kelvin mode amplitude. Through the normal mode decomposition, we will be able to detect spectral regions with significant distortion from the linear behavior caused either by nonlinearities (including the basic state role) and/or forcing.

However, there are some disadvantages to using this approach. For instance, the normal modes of the primitive equations are obtained through the linearization about a basic state at rest and ignoring physical processes such as radiative and diabatic processes and the presence of humidity (Adames et al., 2021; Snide et al., 2021). Such processes might be important in the coupling between waves and convection (Kiladis et al., 2009). In this scenario the effect of the basic state on the atmospheric wave will result from the nonlinear interaction between the waves and the basic states described as a superposition of normal mode functions. Furthermore, the choice of the basis of NMF is not unique, but it is a result of the chosen model, and it has a clear physical interpretation, allowing us to associate particular observed atmospheric oscillations in terms of free-dry atmospheric waves.

### 2.6 Computation of the Low- and High-frequency Intraseasonal in Modal Space

In this work, we used indices that describe the tropical and extratropical precursors associated with the high and low-frequency intraseasonal variability. The resulting precipitation pattern in South America will be assessed in terms of NMF expansion following (Žagar & Franzke, 2015). These authors, for instance, introduced a methodology to decompose the widely-used-all-seasons multivariate MJO index (M. C. Wheeler & Hendon, 2004) into normal mode functions. They performed a linear regression of the RMM indexes $Y_i(t)$, $i = 1, 2$ against the normal mode function coefficients:

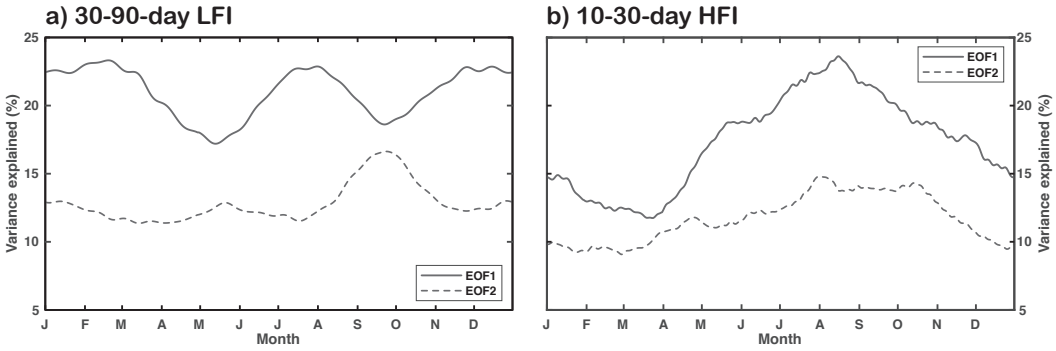


**Figure 2.** Daily eigenvalues corresponding to the EOF analysis of (a) 30-90-day Low-frequency Intraseasonal, and (b) 10-30 High-frequency Intraseasonal filtered OLR. EOFs are calculated between 40°S-5°N and 70°W-30°W (red box in Fig. 1) using a 121-day and 61-day sliding window, respectively.

$$\mathcal{R}^i_{kmn} = \frac{1}{N-1}\sum_{t=1}^{N}\frac{(\chi_{kmn}(t)-\overline{\chi}_{kmn})(Y_i(t)-\overline{Y}_i)}{\mathrm{Var}(Y_i(t))} \tag{14}$$

where $\mathcal{R}^i_{kmn}$ is the regression coefficient of i-th index against the normal mode with mode indices $(k,m,n)$. In addition, the complex coefficient of $\mathcal{R}^i_{kmn}$ describes the projection of the Southern Hemisphere circulation associated with the LFI and HFI index. The relative importance of each normal mode to the given i-th index is obtained by its variance as follow:

$$V^i_{kmn} = gD_m\mathcal{R}^i_{kmn}\left(\mathcal{R}^i_{kmn}\right)^* \tag{15}$$

where $g$ is the acceleration of gravity, $D_m$ is the equivalent depth of the m-th vertical mode [2], and $^*$ indicates the complex conjugate, respectively (more details in (Žagar & Franzke, 2015)).

## 3 EOF results: Seasonal Cycle of the LFI and HFI variability

The spatial pattern associated with both the LFI and HFI variability follows the maximum activity observed in Figure 1 and documented previously (e.g., (C. S. Vera et al., 2018; Gelbrecht et al., 2018; Mayta et al., 2019)). Figure 2a shows the seasonal cycle of EOF1 and EOF2 for each day obtained from the EOF analysis applied to the 30-90-day Low-frequency filtered OLR. The first two modes explain on average about 22% and 12% of the total variance, respectively. These modes are distinct and well-separated from the rest (not shown), following the North's criteria (North et al., 1982). The variance explained by the EOF1 peaks during mid-February, August, and mid-December.

[2] The equivalent depth is the eigenvalue of the vertical structure problem so that each equivalent depth is associated with a different vertical profile. For example, the vertical mode $m = 1$ has the largest equivalent depth $D_1 = 10165.05m$ and corresponds to the external mode (it does not change sign along the vertical coordinate). The vertical modes $m \geq 2$ are internal modes, and they change sign $m - 1$ times along the vertical coordinate $\sigma$.

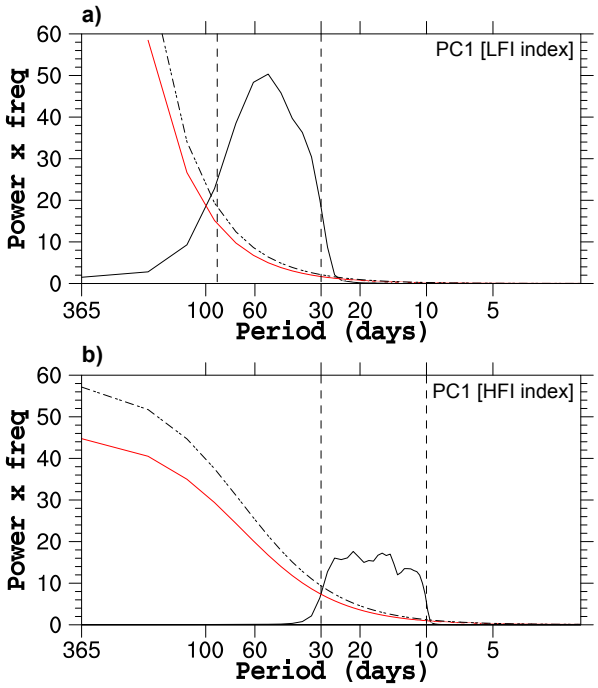


**Figure 3.** Power spectra of the leading first EOF associated with the (a) 30-90-day low-frequency intraseasonal (LFI) and (b) 10-30-day high-frequency intraseasonal (HFI). The red curve is the red-noise spectrum and the black dashed lines are the 95% significance levels.

On the other hand, Fig. 2b shows the seasonal cycle of EOF1 and EOF2 corresponding to the 10-30-day High-frequency filtered OLR. The HFI EOF1 and EOF2 explain on average about 19% and 10% of the total variance, respectively. The variance explained by the HFI EOF1 peaks, as documented by (C. S. Vera et al., 2018)(see their Fig. 4f), during mid-August. Its maximum activity during austral winter yields some clues about how HFI variability in winter plays a key role. This hypothesis will be explored in section 4.3.

Power spectra of the PC1 of the leading EOF1 for the 30-90-day and 10-30-day intraseasonal are shown in Fig. 3. The largeness of the variance of PC1 for the LFI EOF1 is concentrated at intraseasonal periods (30-90 days) typically associated with the large-scale MJO (Kiladis et al., 2005; Adames & Wallace, 2014). The peak of the spectral signal is located at ∼48 days, which is the average period for the MJO cycle around the globe. The bulk of the variance of PC1 for the HFI EOF1, on the other hand, is concentrated for the 10-30-day period. Two spectral peaks are barely observed, one at ∼15, and a second peak at ∼25 days. Similar spectral peaks were also documented in the OLR data for the submonthly time-scale in (Liebmann et al., 1999).

## 4 South America Intraseasonal Variability: Dynamical Mechanisms

### 4.1 South America 30-90-day Low-Frequency Intraseasonal variability (LFI)

Figure 4 shows the composite OLR (shading), velocity potential ($\chi$; contours), and winds (vectors) for LFI over South America at 200 hPa, obtained by regressing these fields

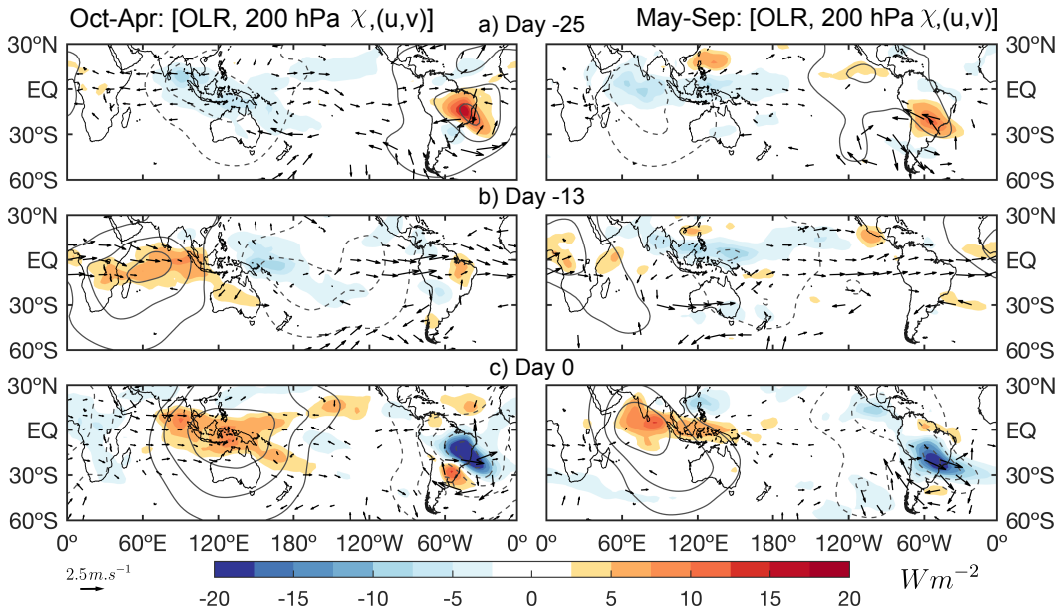


**Figure 4.** Regressed values of OLR (shading), velocity potential ($\chi$; contours), and winds (vectors) at 200-hPa, based on LFI OLR index on day 0. Shaded OLR in W m$^{-2}$ are shown by the legend. The velocity potential contour interval is $7.5\times10^5$ m$^2$s$^{-1}$. Positive (negative) contours are solid (dashed). The reference wind vectors correspond to 2.5 m s$^{-1}$, and are plotted only where either the $u$ or $v$ component is significant at the 95% level or greater.

onto 30-90 PC1 (LFI index) using the methodology outlined in section 2.3. The lags considered in Fig. 4 are based in the spectral peak (around 50 days) observed in Fig. 3a.

Figure 4 depicts the evolution of tropical convection and implied large-scale circulation (upper-level velocity potential and winds) during a typical oscillation for the October-April (left column) and May-September season (right column). The large convection anomalies along the equator in the Maritime continent (Fig. 4a) propagate eastward to South America resulting in the SESA-SACZ dipole-like configuration (Fig. 4c). Despite the EOF calculations are made within the South America domain, the upper-level structure exhibits a zonal wavenumber-1 structure in the equatorial belt as in other EOF-based analyses of the MJO. For instance, at day 0 (Fig. 4c) shows a strong positive center over the Maritime Continent and the negative center of action over South America.

On the other hand, Figure 4 (right column) shows the large-scale convection pattern and upper-level divergence for the May-September period. Some differences in eastward propagation phase speed for the circulation and OLR anomalies are evident in the regression maps. The OLR anomalies, initially over the Maritime Continent (day -25 in Fig. 4a), propagate eastward creating a condition for convection in a broad area of South America (day -25; Fig. 4c). The convective evolution, from day -25 on, shows clear resembles the spatial structure widely documented by using diverse MJO indices (e.g., (M. C. Wheeler & Hendon, 2004; Kiladis et al., 2014)). The upper-level divergence (negative velocity potential) shows a positive center over the Indian Ocean and a more diffuse negative center of action over South America. The convective-dynamical evolution observed during October-April, even during the May-September months, clearly resembles the composite maps made using the OMI index in (Mayta et al., 2020). Because the LFI index was

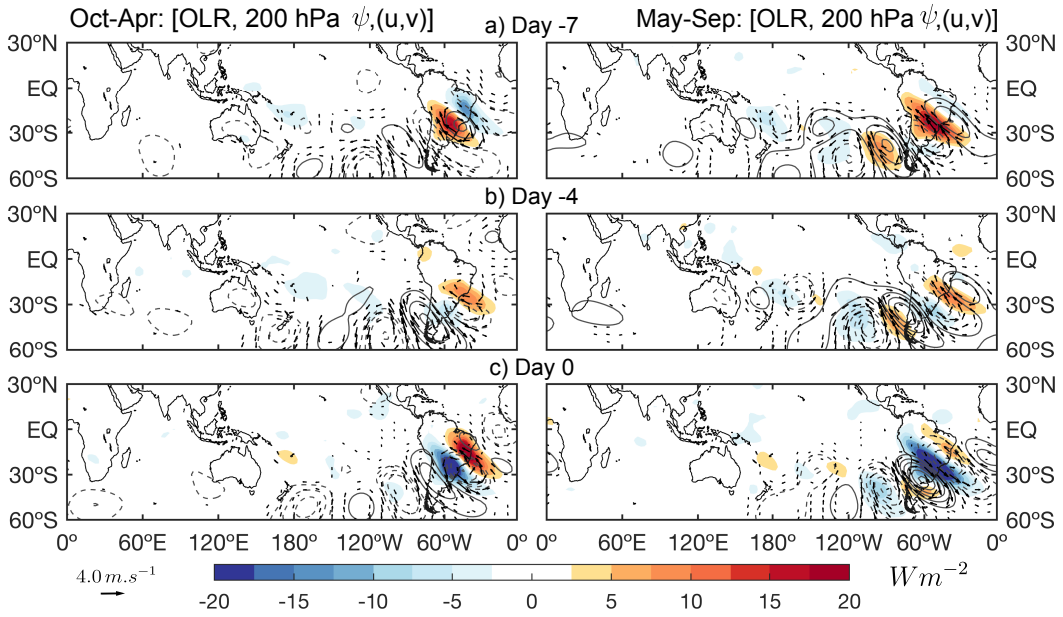


**Figure 5.** Regressed values of OLR (shading), streamfunction ($\psi$; contours), and winds (vectors) at 200-hPa based on 10-30 PC1 (HFI index). Shaded OLR in W m$^{-2}$ are shown by the legend. Streamfunction contour interval is $2\times10^6$ m$^2$ s$^{-1}$. Positive (negative) contours are solid (dashed). The reference wind vectors correspond to 4 m s$^{-1}$, and are plotted only where either the $u$ or $v$ component is significant at the 95% level or greater.

calculated using a sliding window, our results demonstrated that this index properly represents the seasonal large-scale MJO impacts (Kikuchi et al., 2012; Wang et al., 2018).

### 4.2 South America 10-30-day High-Frequency Intraseasonal variability (HFI)

Similarly to the previous section, here the 10-30 PC1 (HFI index) is regressed against dynamical and convective fields. Figure 5 shows the regressed values of OLR (shading), 200 hPa streamfunction (contours), and winds (vectors), based on 10-30 PC1 (HFI index) for days -7, -4, and day 0. The lags considered in Fig. 5 are based in the spectral peak (around 15 days) observed in Fig. 3b. The regression maps are separately calculated for the Oct-Apr (left column) and May-Sep (right column) seasons. During the Oct-Apr period, at day -7, as in (C. S. Vera et al., 2018), suppressed convection occurs over the SESA region (Fig. 5a). At the same time, a well-developed series of upper-level alternating cyclones and anticyclones extending eastward and equatorward are observed. Then, 3 days later, enhanced convection signal starts over Argentina, as the time of the wave trains propagate towards the South Atlantic Ocean (Fig. 5b). At day 0 (Fig. 5c), convection peaks over the SESA region and the Rossby wave train are propagating equatorward. There seem to be two extratropical Rossby wave trains during this season, a subtropical and a subpolar one, reminiscent of the split jet during winter. Our results are consistent with previous works (Kiladis & Weickmann, 1997; Liebmann et al., 1999; Cavalcanti & Kayano, 1999; Carvalho et al., 2004) who showed similar OLR and large-scale features associated with the submonthly variability over the SACZ region.

On the other hand, during the May-Sep season, the suppressed (day -7) and enhanced (day 0) convection cover a broad area of South America with a northwest-southeast

band extending to the adjacent ocean. Recently, (C. S. Vera et al., 2018) also showed similar strong convection over the SESA region extending their signal towards the southern Amazon, as observed in Fig. 5c. Similarly, the convection activity observed during the dry period is accompanied by highly statistically significant Rossby wave trains. The wave trains, unlike the Oct-Apr period, stretches eastward and equatorward from the Western Pacific and South Pacific Convergence Zone (SPCZ) with an arch-like structure. This pattern resembles the spatial features associated with the PSA-like mode documented by (Mo & Higgins, 1998). Many of the extratropical wave trains in the upper-troposphere (Figure 5) are, in many instances, directly forced by the divergent outflow from regions of enhanced equatorial convection, such as the MJO convection (Jin & Hoskins, 1995; Mori & Watanabe, 2008). Moreover, considering that the SPCZ has a broad multiscale variability (Matthews, 2012), including the submonthly timescale, previous studies have already suggested the interactions between convection over South America and the SPCZ through Rossby wave trains (Grimm & Silva Dias, 1995; Gonzalez & Vera, 2014).

Overall, the dipole-like SESA–SACZ precipitation pattern is caused primarily owing to the HFI by the southern hemisphere Rossby waves. Other wave modes to characterize the HFI will be explored in detail in the next sections.

### 4.3 The relationship between the LFI and HFI variability

Recent studies documented that a large part of the intraseasonal SESA-SACZ dipole-like configuration over South America is due to extratropical wave disturbances such as Rossby wave trains (C. S. Vera et al., 2018; Gelbrecht et al., 2018; Mayta et al., 2019). Thus, in this section, the different precursors of the LFI events are assessed. In section 3.1 is detailed how each event and the different precursors are defined. Table 1 summarizes the total LFI events recorded for the 1980-2016 period. In total 147 events were recorded for the entire period, which means around ∼4 per-year. As expected from previous sections, LFI events are mainly associated with the large-scale MJO eastward propagation, responsible for the spatial structure observed in Fig. 4. On average, 70% of the total events are associated with the MJO activity, as also detected by the MJO indices. However, about 20% of these events are mainly preceded by HFI activity. Another important point to stand out is the existence of a significant percent ($\sim$ 20%) of occurrences of LFI events preceded by tropical and extratropical precursors acting simultaneously. Even though the HFI events show an almost constant activity throughout the year (not shown), these events play an important role in organizing convection mainly during the dry season. The remaining events, as appears in Table 1, are explained by other precursors. Other precursors could be associated, for instance, with disturbances that act at the same frequency, such as the westward propagating Rossby equatorial waves (M. Wheeler & Kiladis, 1999; M. C. Wheeler et al., 2000). Indeed, even events with tropical precursors in many instances could be associated with the convectively-coupled Kelvin waves (Liebmann et al., 2009). Finally, we observed a deficit of LFI events during the El Niño years (e.g., 1986/87, 1997/98, 2009/10) and the exceptional warm SST conditions in the tropical Atlantic, occurred in 2005 and 2010 (Table 1).

In the next section, we will use a normal mode decomposition of the LFI and HFI to describe the modal structure as well as the horizontal and vertical scales of the perturbations associated with both indices.

## 5 Normal-modes Components of the South America intraseasonal variability

The interaction between tropical convection and large-scale systems is characterized by energy conversion processes (Silva Dias et al., 1983). In this sense, the analysis of normal-modes decomposition of the intraseasonal variability constitutes a methodology for diagnosing the energy responsible for the circulation. In this approach, the so-

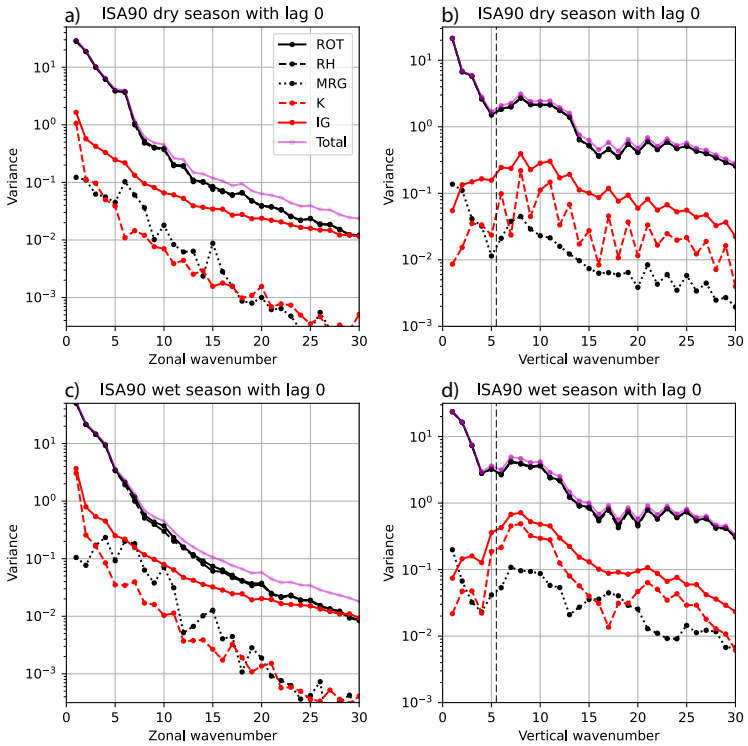


**Figure 6.** The LFI index variance explained by zonal (left column) and vertical (right column) mode. The variance at the top (bottom) corresponds to the May–September (October–April) period. Dashed lines separate the "tropospheric equivalent barotropic modes" and the baroclinic modes.

lution of the vertical structure associated with intraseasonal variability makes it possible to analyze the energetics for each of the vertical modes, separately, in external and internal modes (Figures 6,8). While in the energy distribution between the horizontal modes (Figures 7, 9, and A1), the eigenvalues (normal modes) are classified in modes gravitational (Kelvin and gravity waves; IGW) and rotational (Rossby and mixed waves; ROT).

### 5.1 Normal-modes Components: 30-90-days LFI

Figure 6 displays the contribution of each mode (zonal and vertical) to the total variance. On large-scales ($k$=1–5) most of the LFI index variance is well-described by Rossby modes, with non-negligible contributions of Kelvin and Mixed Rossby-gravity modes accounting for about 10% of the variance. Our results are in agreement with (Žagar & Franzke, 2015), where the authors documented the same planetary modes for the MJO. For more internal modes (lower equivalent depth), the contribution of inertio-gravity waves becomes more comparable and in the same order as Rossby modes. It is also observed similar LFI-associated modes for both the May to Sep and Oct-Apr periods.

Figures 6b,d reveal the leading vertical modes with a strong contribution of tropospheric equivalent barotropic modes[3], while barotropic Kelvin and inertio-gravity modes

[3] In this study, we call a barotropic mode every mode with an equivalent barotropic structure in the troposphere.

are less prevalent since these modes are associated with large-scale convection. Baroclinic Rossby modes, although still prevalent, account for less variance than the barotropic ones, while the contribution of baroclinic Kelvin waves becomes more important (especially for $m$=7–11). The distribution of variance is similar throughout both wet and dry seasons. The most noticeable difference is the larger contribution of Kelvin waves during the wet season, which was also expected (Figure 6c).

Figure 7 shows the regression horizontal structure associated with the LFI index for a pressure level close to ∼200–hPa. The projected circulation represents the contribution of the rotational modes (ROT, Fig. 7a,d), inertio-gravity modes (IGW, Fig. 7b,e), and the total fields (Fig. 7c,f). The calculations are computed separately for the October-April and May-September season, respectively, and at lag 0 only (as in Fig. 4c). Figures 7c,f suggest that majority of LFI circulation, such as the mid-latitude wave-trains, is dominated by ROT modes. However, for the MJO large-scale, the ROT mode ($k$=1 Rossby wave) is the dominant mode associated with the MJO (Žagar & Franzke, 2015). These wide-documented mid-latitude wave-trains (e.g., (C. S. Vera et al., 2018; Gelbrecht et al., 2018), and references therein) present different aspects comparing the dry and wet seasons that can be explained in terms of the spectrum of their ROT variance in each season (Figure 6). Indeed, these wave-trains acquire a more clear pattern in the dry season, since in this season there is less energy in global scale wave-numbers $k = 0 - 3$ and more energy in wave-numbers $k = 4 - 6$ when compared to the wet season. This result was also expected since the dominant LFI pattern from May-September is mainly influenced by the extratropical disturbances rather than large-scale MJO eastward-propagation (Fig. 4 and Table 1). Figure 4b also depicts westerly winds along the equator ahead of the region of strong convection (South America) resembling the structure of the $k = 1$ eastward propagating IGW mode (i.e., the Kelvin wave). Indeed, as observed in Figure 6c for the wet season, the contribution of Kelvin waves within IGW decay rapidly, and therefore within the total fields as well. A relatively strong IGW signal over the Andes, as observed in Fig. 7e, is a result of its interaction with the Southern Hemisphere winter upper-level westerlies that are stronger at this latitude. To better represent the MJO upper-level zonal wavenumber-1 ($k$=1) structure in the equatorial belt, we plotted in Figure A1 the velocity potential instead of streamfunction. The upper-level wind anomalies are mainly zonal (Fig. A1b) with a wavenumber-1 structure comparable to those in previous studies of (Hendon & Liebmann, 1994; Kiladis et al., 2005; Adames & Wallace, 2014). The pattern is suggestive of an equatorial Kelvin wave signature that extends from South America, being barely equatorially trapped with a band of westerlies between 10°N/S. On the other hand, upper-level divergence over South America, even in IG modes, highlights the presence of wave trains (Fig. A1e).

### 5.2 Normal-modes Components: 10-30-days HFI

Following equation 15, Figure 8 shows the contribution of the various modes to the HFI index. The results show that the distribution of the variance of the regression coefficients is dominated by rotational modes. For instance, the variance distribution on the zonal mode index $k$ shows that HFI is strongly dominated by Rossby modes for large-scale modes ($k$=1-7). However, the contribution of the Rossby mode presents a fast decay as $k$ increases in a way that for smaller-scale modes (i.e., $k \geq 15$) when the contribution of inertio-gravity waves become more relevant. On the other hand, as expected, the contribution of equatorially confined modes such as Kelvin and mixed Rossby-gravity modes are less relevant compared to their contribution to LFI (Figures 8a, c).

The vertical distribution of the variance shows that HFI variability is more associated with modes with barotropic structure in the troposphere ($m$=1-5; Fig. 8b, d). Considering that HFI represents here higher latitudes dynamics, lower-order modes, with the barotropic mode becoming dominant, were expected (Kasahara & Puri, 1981; Silva Dias & Bonatti, 1985). In addition, a strong contribution of modes with baroclinic structure

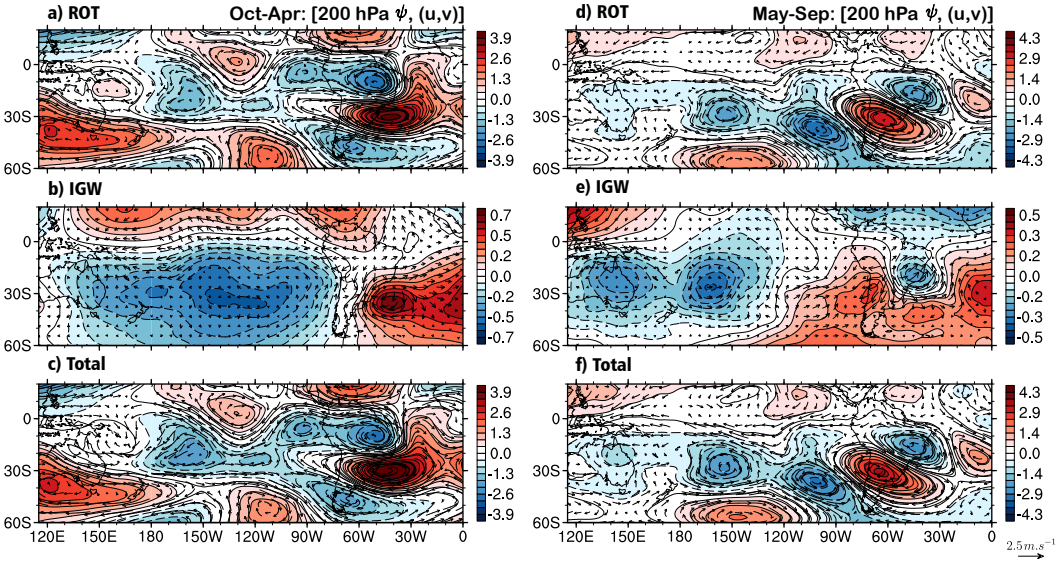


**Figure 7.** Low-frequency intraseasonal (LFI) regression patterns of upper-level (200-hPa) winds (vectors) and streamfunction (filled contours). (a), (d) are rotational components; (b), (e) are inertio-gravity components; and (c), (f) are the total fields. Regressions patterns in the left (right) column corresponds to the October-April (May-September) period. Streamfunction contour interval is 1x10$^6$ m$^2$ s$^{-1}$. Positive (negative) values are shown in red (blue). The reference wind vectors correspond to 2.5 m s$^{-1}$.

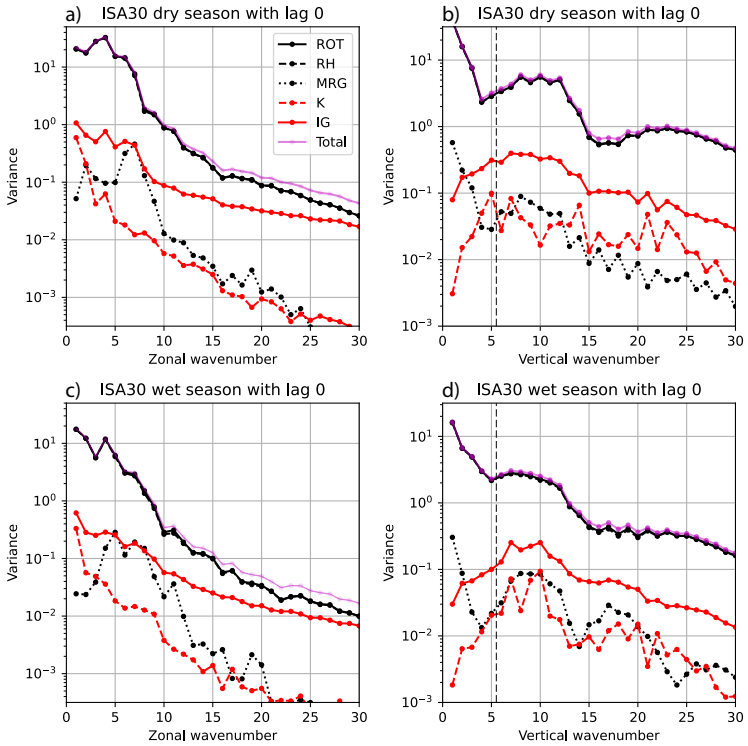


**Figure 8.** As in Figure 6, but for the HFI index.

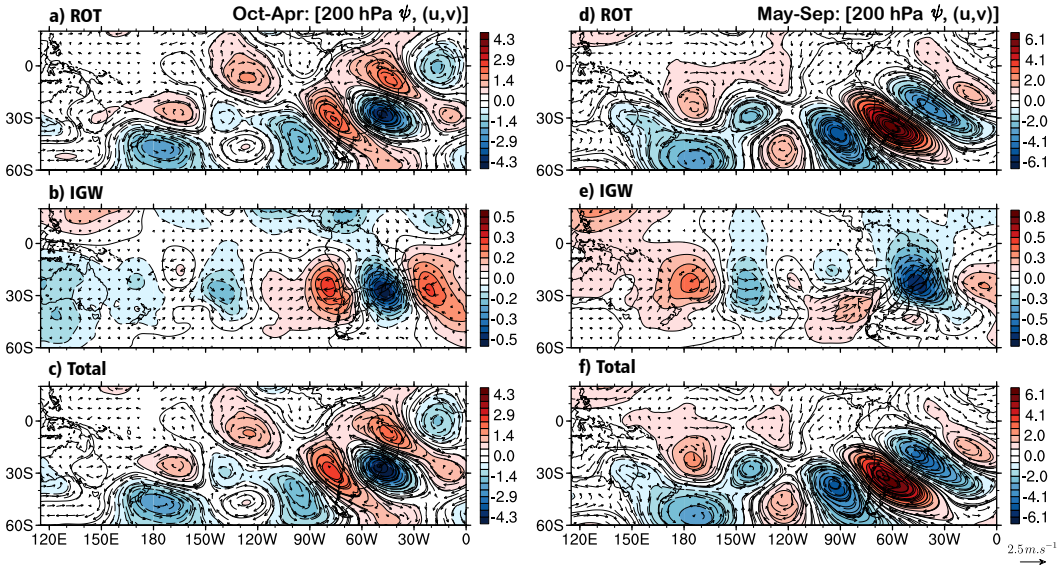


**Figure 9.** As in Figure 7, but for the HFI index.

is observed in modes with large $m$ ($m$=6-15), with peaks at $m$=8-9. Peaks at $m$=8-9 are quite evident for both seasons, stronger during the May-Sept period, as also documented in (Silva Dias & Bonatti, 1985). Differences in the distribution of variance with the mode index are very similar in both dry and wet seasons. The most significant difference noticed is the larger contribution of Mixed Rossby-Gravity (MRG) modes during the dry season (Figures 8b, d). Indeed, it could be explained by the fact that this mode has an asymmetric wind structure with respect to the equator and can have different responses owing to solar forcing depending on the time of the year (Silva Dias et al., 1983).

The decomposition of the regressed circulation fields (upper-level streamfunction and winds) onto IGW and ROT components associated with HFI is presented in Figure 9. According to Figures 9c, f the average HFI circulation is rotational, which is also expected from Figure 8. In other words, we can reconstruct the basic features of the previously observed structures in Figure 5 using just rotational modes. The same predominance by rotational modes is found for both seasons. Comparing with the pattern of the regressed LFI fields, on the other hand, it is noticeable that IGW modes have a more important contribution of wave-numbers $k$=4-7, rather than the rapidly decaying variance of the IGW modes associated with LFI.

## 6 Equatorial Mode Contribution in the LFI Evolution: A case study

Figure 10 shows a time-longitude diagram of the OLR and the reconstructed velocity potential and streamfunction for the LFI events identified during January to March of 1995. The envelope of enhanced convection (negative OLR anomalies) can be seen to propagate eastward from equatorial Africa to the western Pacific (Fig. 10g). At the time of convection reach the cold pool and tropical South America region, it propagates faster and the associated OLR is weaker. Over the Indo-West Pacific warm pool is clear that the IGW modes such as Kelvin mode (Figs. 10a, c) play an important role in the structure observed in the OLR anomalies. Over tropical South America, despite the convection and circulations are averaged along the equatorial belt (from 5°S to 5°N), the convective features appear to be more influenced by ROT modes. The study case also shows a clear longitudinal contrast: where the ROT modes dominate, the IGW modes do not and vice versa (Figs. 10a and 10d). These results yield clues about the lack of skill of

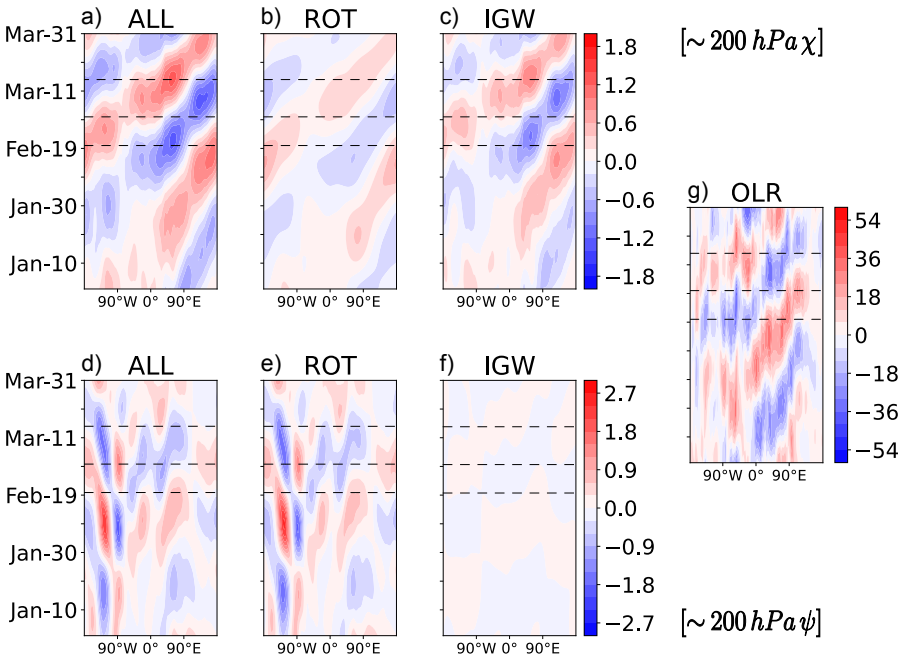


**Figure 10.** Time-longitude diagram of 30-90-day filtered (∼ 200 hPa) velocity potential ($\chi$, top panels), streamfunction ($\psi$, bottom panels), and OLR averaged from 5°S to 5°N. The y-axis is the time from January to March 1990 of the LFI event shown in Table 1. Positive (negative) anomalies are red (blue) with contour intervals shown by the legend.

the global MJO indices commonly used for monitoring intraseasonal precipitation (see Table 1). Similar issues of the diverse global MJO indices were documented in detail in previous works (e.g., (Mayta et al., 2020)).

From the results above, including the case study, we find that the IGW mode (e.g., Kelvin wave) is the dominant mode associated with the MJO global structure over the Indo-West Pacific warm pool, while ROT modes are "regionally" more important. Figures S1 to S3, for instance, show the lag-regression between the LFI index and the IGW and ROT modes, in order to analyze if tropical convection trigger mid-latitude Rossby waves. During the wet season (Fig. S3a), is possible to observe that tropical convection excites a significant response in the IGW and Rossby waves. The lag correlation analysis also depicts that the IGW modes reach larger lag-correlation values (within about 15-10 days) than the Rossby waves (10-5 days). This relatively "slow" response in the IGW modes constitutes an inherent part of the eastward MJO propagation (tropical-tropical teleconnection), despite a decoupled with convection is observed in the cold pool region. On the other hand, the "quick" response in the Rossby waves is consistent with what was found in previous works (Franzke et al., 2019; Grimm, 2019), where the extratropical response to tropical heating anomalies reaches its maximum amplitude after 5-7 days.

## 7 Summary and Conclusions

In this study, we presented an alternative approach to analyzing subtropical and extratropical South American intraseasonal variability, based on normal mode decomposition. This methodology involves decomposition of circulation and pressure fields into normal-mode functions (NMF), which was applied in previous studies to the MJO (Žagar

et al., 2015; Franzke et al., 2019). In particular, we focus on the interaction between mid-latitude wave disturbances and the classical equatorial MJO impact in the intraseasonal signal over South America.

We started by separating intraseasonal South America variability into 30-90-day Low-Frequency Intraseasonal (LFI), and 10–30-day High-Frequency Intraseasonal (HFI) as in (C. S. Vera et al., 2018). For LFI and HFI, the leading patterns were studied through EOF analysis as in (Kiladis et al., 2014). EOFs were computed onto the region of maximum intraseasonal signal indicated by the red box in Figure 1. The period considered for the analysis was from 1980 to 2016, but centered on each day of the calendar year, using a sliding window approach to take into account the seasonal migration of the intraseasonal signal (Kiladis et al., 2014; Wang et al., 2018).

The results show that the PC1 (dominant mode for both LFI and HFI; Figure 2) time series describes well the intraseasonal variability in South America. Considering the LFI, the presence of a dipole-like SESA-SACZ structure (Casarin & Kousky, 1986; Nogués-Paegle & Mo, 1997; C. S. Vera et al., 2018; Gelbrecht et al., 2018) is the most distinctive feature observed over South America during the wet season (Oct–Apr). This structure, as documented in the references above, is primarily caused by the large-scale eastward-moving MJO (Figure 4). LFI events showed maximum activity during the wet season, where events preceded by the MJO are well-described by different MJO indices (Table 1). Even though during the May–Sep season an apparent presence of the large-scale MJO (Fig. 4) is observed, the enhanced convection over the SESA region is mainly controlled by extratropical wave disturbances (Table 1). Our results, on the other hand, demonstrated that the HFI spatial pattern also resembles the so-called SESA–SACZ structure, in response to the Rossby wave trains as in (Grimm & Silva Dias, 1995; C. S. Vera et al., 2018; Grimm, 2019). In addition, HFI events show an almost constant activity throughout the year, playing an important role mainly during the dry season. We found that on average about 20% of the LFI events are preceded by HFI events. Another 20% of the events enhanced convection is preceded by both precursors (Table 1). These results showed, from a statistical point of view, that tropical convection might excite a significant response in the extratropical Rossby wave trains. Mainly, when the enhanced convection is over the Maritime Continent and the South Pacific Convergence Zone, as documented in previous works (Grimm & Silva Dias, 1995; Grimm, 2019).

The relative importance of the rotational (ROT) and inertio-gravity (IGW) components in the South American intraseasonal (LFI and HFI) circulation signature was also assessed in the present study. Using a linear regression between the complex expansion coefficients of the NMF representation of the reanalysis data and daily values of the LFI index, our results show that ROT modes (e.g., Rossby wave) are the most important mode contributing to the tropospheric circulation and the SESA–SACZ convective structure observed over South America (Figures 6, 7, A1, S1, and S2). This relationship is clearly observed for the case study depicted in Fig. 10. Despite the IGW mode such as Kelvin wave is the dominant mode associated with the MJO global structure over the Indo-West Pacific warm pool region, ROT modes (e.g., Rossby waves) are "regionally" more important (Figs. 10 and S3). Less important was the contribution of the IGW modes (e.g., Kelvin mode), prevailing mainly during the wet season (Figures 6c, 9b, A1b). In addition, zonal and vertical mode contribution to the total variance revealed a strong contribution of barotropic modes rather than other vertical modes (Figure 6a, b). Considering that the South America Monsoon System constitutes an important heat source, our results also yield clues about the preferential interaction between the intraseasonal time scale and others, for instance through tropical- extra-tropical interactions of the normal modes (C. F. M. Raupp et al., 2008). We find a significant wave response in the mid-latitude Rossby waves, which is consistent with what was found in previous works (Franzke et al., 2019; Grimm, 2019), where the extratropical response to tropical heating anomalies reaches its maximum amplitude after 10–7 days (Fig. S3). HFI variability (Fig. 5),

on the other hand, as was depicted for LFI, is dominated by rotational modes throughout the year (Figure 8).

Subseasonal to intraseasonal variability over South America involves a complex and nonlinear interaction between them. The normal mode approach is, indeed, an alternative way of evaluating the intraseasonal variability over South America. The proposed decomposition methodology of low- and high-frequency intraseasonal can provides insights into the dynamics of the intraseasonal variability in South America, providing a powerful tool for diagnosing model problems when comparing normal mode decomposition of reanalysis and model predictions of precipitation.

## Acknowledgments

VM was supported by the National Science Foundation under Grant AGS-1841559. ASWT was supported by FAPESP (Fundação de Amparo à Pesquisa do Estado de São Paulo) under grant 2020/14162-6. Interpolated OLR data is provided by the NOAA/ESRL at `https://psl.noaa.gov/data/gridded/data.interp_OLR.html`. Reanalysis data is available at `https://cds.climate.copernicus.eu/`. The open software MODES can be found at `https://modes.cen.uni-hamburg.de/modes-software`. Different MJO indices used in this study are also available at `https://psl.noaa.gov/mjo/mjoindex/`.

## References

Adames, A. F., Powell, S. W., Ahmed, F., Mayta, V. C., & Neelin, J. D. (2021). Tropical Precipitation Evolution in a Buoyancy-Budget Framework. *Journal of the Atmospheric Sciences*, *78*(2), 509 - 528. doi: 10.1175/JAS-D-20-0074.1

Adames, A. F., & Wallace, J. M. (2014). Three-dimensional structure and evolution of the mjo and its relation to the mean flow. *Journal of the Atmospheric Sciences*, *71*(6), 2007-2026. doi: 10.1175/JAS-D-13-0254.1

Alvarez, M. S., Vera, C. S., & Kiladis, G. N. (2017). Mjo modulating the activity of the leading mode of intraseasonal variability in south america. *Atmosphere*, *8*(12). Retrieved from `https://www.mdpi.com/2073-4433/8/12/232`

Alvarez, M. S., Vera, C. S., Kiladis, G. N., & Liebmann, B. (2016, Jan 01). Influence of the madden julian oscillation on precipitation and surface air temperature in south america. *Climate Dynamics*, *46*(1), 245–262.

Ambrizzi, T., & Hoskins, B. J. (1997). Stationary rossby-wave propagation in a baroclinic atmosphere. *Quarterly Journal of the Royal Meteorological Society*, *123*(540), 919-928. doi: 10.1002/qj.49712354007

Baer, F. (1972, 05). An Alternate Scale Representation of Atmospheric Energy Spectra. *Journal of the Atmospheric Sciences*, *29*(4), 649-664. doi: 10.1175/1520-0469(1972)029⟨0649:AASROA⟩2.0.CO;2

Carvalho, L. M. V., Jones, C., & Liebmann, B. (2004). The south atlantic convergence zone: Intensity, form, persistence, and relationships with intraseasonal to interannual activity and extreme rainfall. *Journal of Climate*, *17*(1), 88-108. doi: 10.1175/1520-0442(2004)017⟨0088:TSACZI⟩2.0.CO;2

Casarin, D. P., & Kousky, V. E. (1986). Anomalias de precipitação no sul do brasil e variações na circulação atmosférica. *Revista Brasileira de Meteorologia*, *2*, 83-90.

Castanheira, J. M., & Marques, C. A. F. (2015). Convectively coupled equatorial-wave diagnosis using three-dimensional normal modes. *Quarterly Journal of the Royal Meteorological Society*, *141*(692), 2776-2792. doi: 10.1002/qj.2563

Cavalcanti, I. F. A., & Kayano, M. T. (1999). High-frequency patterns of the atmospheric circulation over the southern hemisphere and South America. *Meteorology and Atmospheric Physics*, *69*(3-4), 179–193. doi: 10.1007/BF01030420

Chu, J.-E., Wang, B., Lee, J.-Y., & Ha, K.-J. (2017). Boreal Summer Intrasea-

sonal Phases Identified by Nonlinear Multivariate Empirical Orthogonal Function–Based Self-Organizing Map (ESOM) Analysis. *Journal of Climate*, *30*(10), 3513-3528. doi: 10.1175/JCLI-D-16-0660.1

Cunningham, C., & Cavalcanti, I. F. A. (2006). Intraseasonal modes of variability affecting the south atlantic convergence zone. *International Journal of Climatology*, *26*(9), 1165-1180. doi: 10.1002/joc.1309

Franzke, C. L. E., Jelic, D., Lee, S., & Feldstein, S. B. (2019). Systematic decomposition of the mjo and its northern hemispheric extratropical response into rossby and inertio-gravity components. *Quarterly Journal of the Royal Meteorological Society*, *145*(720), 1147-1164. doi: 10.1002/qj.3484

Garreaud, R. D. (2000). Cold air incursions over subtropical south america: Mean structure and dynamics. *Monthly Weather Review*, *128*(7), 2544-2559. doi: 10.1175/1520-0493(2000)128⟨2544:CAIOSS⟩2.0.CO;2

Garreaud, R. D., & Wallace, J. M. (1998). Summertime incursions of midlatitude air into subtropical and tropical south america. *Monthly Weather Review*, *126*(10), 2713-2733. doi: 10.1175/1520-0493(1998)126⟨2713:SIOMAI⟩2.0.CO;2

Gelbrecht, M., Boers, N., & Kurths, J. (2018). Phase coherence between precipitation in south america and rossby waves. *Science Advances*, *4*(12). doi: 10.1126/sciadv.aau3191

Gonzalez, P. L. M., & Vera, C. S. (2014, Oct 01). Summer precipitation variability over south america on long and short intraseasonal timescales. *Climate Dynamics*, *43*(7), 1993–2007. doi: 10.1007/s00382-013-2023-2

Grimm, A. M. (2019). Madden–Julian Oscillation impacts on South American summer monsoon season: precipitation anomalies, extreme events, teleconnections, and role in the MJO cycle. *Climate Dynamics*, *53*(1-2), 907–932. doi: 10.1007/s00382-019-04622-6

Grimm, A. M., & Silva Dias, P. L. (1995). Analysis of tropical-extratropical interactions with influence functions of a barotropic model. *Journal of the Atmospheric Sciences*, *52*(20), 3538-3555. doi: 10.1175/1520-0469(1995)052⟨3538:AOTIWI⟩2.0.CO;2

Hendon, H. H., & Liebmann, B. (1994). Organization of convection within the Madden-Julian oscillation. *J. Geophys. Res.*, *99*(D4), 8073–8083.

Hersbach, H., Bell, W., Berrisford, P., Horányi, A., J., M.-S., Nicolas, J., ... Dee, D. (2019, 04). Global reanalysis: goodbye era-interim, hello era5. , 17-24. Retrieved from `https://www.ecmwf.int/node/19027` doi: 10.21957/vf291hehd7

Jin, F., & Hoskins, B. J. (1995). The direct response to tropical heating in a baroclinic atmosphere. *Journal of the Atmospheric Sciences*, *52*(3), 307-319. doi: 10.1175/1520-0469(1995)052⟨0307:TDRTTH⟩2.0.CO;2

Jones, C., & Carvalho, L. M. V. (2002). Active and break phases in the south american monsoon system. *Journal of Climate*, *15*(8), 905-914. doi: 10.1175/1520-0442(2002)015⟨0905:AABPIT⟩2.0.CO;2

Kasahara, A. (1980). Effect of zonal flows on the free oscillations of a barotropic atmosphere. *Journal of the Atmospheric Sciences*, *37*(5), 917-929. doi: 10.1175/1520-0469(1980)037⟨0917:EOZFOT⟩2.0.CO;2

Kasahara, A., & Puri, K. (1981). Spectral representation of three-dimensional global data by expansion in normal mode functions. *Monthly Weather Review*, *109*(1), 37-51.

Kikuchi, K., Wang, B., & Kajikawa, Y. (2012). Bimodal representation of the tropical intraseasonal oscillation. *Clim. Dyn.*, *10*, 1989–2000.

Kiladis, G. N., Dias, J., Straub, K. H., Wheeler, M. C., Tulich, S. N., Kikuchi, K., ... Ventrice, M. J. (2014, 2014/05/29). A comparison of OLR and circulation-based indices for tracking the MJO. *Monthly Weather Review*, *142*(5), 1697–1715. doi: 10.1175/MWR-D-13-00301.1

Kiladis, G. N., Straub, K. H., & Haertel, P. T. (2005, 08). Zonal and Vertical Struc-

ture of the Madden–Julian Oscillation. *Journal of the Atmospheric Sciences*, *62*(8), 2790-2809. doi: 10.1175/JAS3520.1

Kiladis, G. N., & Weickmann, K. M. (1992, 2014/05/29). Circulation anomalies associated with tropical convection during northern winter. *Monthly Weather Review*, *120*(9), 1900–1923. doi: 10.1175/1520-0493(1992)120⟨1900:CAAWTC⟩2.0.CO;2

Kiladis, G. N., & Weickmann, K. M. (1997). Horizontal structure and seasonality of large-scale circulations associated with submonthly tropical convection. *Monthly Weather Review*, *125*(9), 1997–2013. doi: 10.1175/1520-0493(1997)125⟨1997:HSASOL⟩2.0.CO;2

Kiladis, G. N., Wheeler, M. C., Haertel, P. T., Straub, K. H., & Roundy, P. E. (2009). Convectively coupled equatorial waves. *Rev. Geophys.*, *47*(2).

Kitsios, V., O'Kane, T. J., & Žagar, N. (2019, 07). A Reduced-Order Representation of the Madden–Julian Oscillation Based on Reanalyzed Normal Mode Coherences. *Journal of the Atmospheric Sciences*, *76*(8), 2463-2480. doi: 10.1175/JAS-D-18-0197.1

Liebmann, B., Kiladis, G. N., Allured, D., Vera, C. S., Jones, C., Carvalho, L. M. V., ... Gonzales, P. L. M. (2011). Mechanisms associated with large daily rainfall events in northeast brazil. *Journal of Climate*, *24*(2), 376-396. doi: 10.1175/2010JCLI3457.1

Liebmann, B., Kiladis, G. N., Carvalho, L. M. V., Jones, C., Vera, C. S., Bladé, I., & Allured, D. (2009, 2014/05/29). Origin of convectively coupled kelvin waves over south america. *Journal of Climate*, *22*(2), 300–315. doi: 10.1175/2008JCLI2340.1

Liebmann, B., Kiladis, G. N., Marengo, J., Ambrizzi, T., & Glick, J. D. (1999, 2014/05/29). Submonthly convective variability over south america and the south atlantic convergence zone. *Journal of Climate*, *12*(7), 1877–1891. doi: 10.1175/1520-0442(1999)012⟨1877:SCVOSA⟩2.0.CO;2

Liebmann, B., & Smith, C. A. (1996). Description of a complete (interpolated) outgoing long-wave radiation dataset. *Bull. Amer. Meteor. Soc.*, *77*, 1275–1277.

Livezey, R. E., & Chen, W. Y. (1983). Statistical field significance and its determination by Monte Carlo techniques. *Mon. Wea. Rev.*, *111*, 46-59.

Lupo, A. R., Nocera, J. J., Bosart, L. F., Hoffman, E. G., & Knight, D. J. (2001). South american cold surges: Types, composites, and case studies. *Monthly Weather Review*, *129*(5), 1021-1041. doi: 10.1175/1520-0493(2001)129⟨1021:SACSTC⟩2.0.CO;2

Matthews, A. J. (2012). A multiscale framework for the origin and variability of the south pacific convergence zone. *Quarterly Journal of the Royal Meteorological Society*, *138*(666), 1165-1178. doi: 10.1002/qj.1870

Mayta, V. C., Ambrizzi, T., Espinoza, J. C., & Silva Dias, P. L. (2019). The role of the madden-julian oscillation on the amazon basin intraseasonal rainfall variability. *International Journal of Climatology*, *39*(1), 343-360. doi: 10.1002/joc.5810

Mayta, V. C., Kiladis, G. N., Dias, J., Dias, P. L. S., & Gehne, M. (2021). Convectively Coupled Kelvin Waves Over Tropical South America. *Journal of Climate*, *34*(16), 6531-6547. doi: 10.1175/JCLI-D-20-0662.1

Mayta, V. C., Silva, N. P., Ambrizzi, T., Dias, P. L. S., & Espinoza, J. C. (2020). Assessing the skill of all-season diverse Madden–Julian oscillation indices for the intraseasonal Amazon precipitation. *Climate Dynamics*, *54*(7-8), 3729–3749. doi: 10.1007/s00382-020-05202-9

Mo, K. C., & Higgins, R. W. (1998). The pacific–south american modes and tropical convection during the southern hemisphere winter. *Monthly Weather Review*, *126*(6), 1581-1596. doi: 10.1175/1520-0493(1998)126⟨1581:TPSAMA⟩2.0.CO;2

Mori, M., & Watanabe, M. (2008). The growth and triggering mechanisms of the

pna: A mjo-pna coherence. *Journal of the Meteorological Society of Japan. Ser. II*, *86*(1), 213-236. doi: 10.2151/jmsj.86.213

Nogués-Paegle, J., & Mo, K. C. (1997). Alternating wet and dry conditions over south america during summer. *Monthly Weather Review*, *125*(2), 279-291. doi: 10.1175/1520-0493(1997)125⟨0279:AWADCO⟩2.0.CO;2

North, G. R., Bell, T. L., Cahalan, R. F., & Moeng, F. J. (1982). Sampling errors in the estimation of empirical orthogonal functions. *Mon. Wea. Rev.*, *110*, 699–706.

Paegle, J. N., Byerle, L. A., & Mo, K. C. (2000). Intraseasonal modulation of south american summer precipitation. *Monthly Weather Review*, *128*(3), 837-850. doi: 10.1175/1520-0493(2000)128⟨0837:IMOSAS⟩2.0.CO;2

Ramirez, E., da Silva Dias, P. L., & Raupp, C. F. M. (2017). Multiscale atmosphere-ocean interactions and the low-frequency variability in the equatorial region. *Journal of the Atmospheric Sciences*, *74*(8), 2503-2523. doi: 10.1175/JAS-D-15-0325.1

Raphaldini, B., Wakate Teruya, A. S., Silva Dias, P. L., C. Mayta, V., & Takara, V. J. (2020). Normal mode perspective on the 2016 qbo disruption: Evidence for a basic state regime transition. *Geophysical Research Letters*, *47*(14), e2020GL087274. doi: 10.1029/2020GL087274

Raupp, C., & Silva Dias, P. (2010). Interaction of equatorial waves through resonance with the diurnal cycle of tropical heating. *Tellus A*, *62*(5).

Raupp, C. F. M., Dias, P. L. S., Tabak, E. G., & Milewski, P. (2008). Resonant wave interactions in the equatorial waveguide. *J. Atmos. Sci*, *65*(11), 3398–3418.

Raupp, C. F. M., & Silva Dias, P. L. (2009, 2014/06/02). Resonant wave interactions in the presence of a diurnally varying heat source. *Journal of the Atmospheric Sciences*, *66*(10), 3165–3183. doi: 10.1175/2009JAS2899.1

Satyamurty, P., Nobre, C. A., & Silva Dias, P. L. (1998). *South America* (D. J. Karoly & D. G. Vincent, Eds.). Boston, MA: American Meteorological Society. doi: 10.1007/978-1-935704-10-25

Silva Dias, P. L., & Bonatti, J. P. (1985). A preliminary study of the observed vertical mode structure of the summer circulation over tropical south america. *Tellus A: Dynamic Meteorology and Oceanography*, *37*(2), 185-195. doi: 10.3402/tellusa.v37i2.11665

Silva Dias, P. L., Schubert, W. H., & DeMaria, M. (1983). Large-scale response of the tropical atmosphere to transient convection. *Journal of the Atmospheric Sciences*, *40*(11), 2689–2707.

Snide, C. E., Adames, Á. F., Powell, S. W., & Mayta, V. C. (2021). The role of large-scale moistening by adiabatic lifting in the Madden-Julian Oscillation convective onset. *Journal of Climate*.

Souza, E. B., & Ambrizzi, T. (2006). Modulation of the intraseasonal rainfall over tropical brazil by the madden-julian oscillation. *International Journal of Climatology*, *26*(13), 1759-1776. doi: 10.1002/joc.1331

Tanaka, H. (1985). Global energetics analysis by expansion into three-dimensional normal mode functions during the fgge winter. *Journal of the Meteorological Society of Japan. Ser. II*, *63*(2), 180-200. doi: 10.2151/jmsj1965.63.2_180

Vera, C., Higgins, W., Amador, J., Ambrizzi, T., Garreaud, R., Gochis, D., ... Zhang, C. (2006). Toward a unified view of the american monsoon systems. *Journal of Climate*, *19*(20), 4977-5000. doi: 10.1175/JCLI3896.1

Vera, C. S., Alvarez, M. S., Gonzalez, P. L. M., Liebmann, B., & Kiladis, G. N. (2018, Sep 01). Seasonal cycle of precipitation variability in south america on intraseasonal timescales. *Climate Dynamics*, *51*(5), 1991–2001.

Wang, S., Ma, D., Sobel, A. H., & Tippett, M. K. (2018). Propagation characteristics of bsiso indices. *Geophysical Research Letters*, *45*(18), 9934-9943. doi: 10.1029/2018GL078321

Wheeler, M., & Kiladis, G. (1999). Convectively-coupled equatorial waves: Analysis of clouds in the wavenumber-frequency domain. *J. Atmos. Sci.*, *56*, 374–399.

Wheeler, M. C., & Hendon, H. H. (2004). An all-season real-time multivariate MJO index: Development of an index for monitoring and prediction. *Mon. Wea. Rev*, *132*(8), 1917–1932.

Wheeler, M. C., Kiladis, G. N., & Webster, P. J. (2000). Large-scale dynamical fields associated with convectively coupled equatorial waves. *Journal of the Atmospheric Sciences*, *57*(5), 613–640.

Žagar, N., & Franzke, C. L. (2015). Systematic decomposition of the madden-julian oscillation into balanced and inertio-gravity components. *Geophysical Research Letters*, *42*(16), 6829–6835.

Žagar, N., Kasahara, A., Terasaki, K., Tribbia, J., & Tanaka, H. (2015). Normal-mode function representation of global 3-D data sets: open-access software for the atmospheric research community. *Geoscientific Model Development*, *8*(4), 1169–1195. doi: 10.5194/gmd-8-1169-2015

## Appendix A Observed Upper-level Horizontal structure

Figure A1 shows the regressed OLR and circulation at 200 hPa using the 30-90 PC1. The corresponding pattern at 200 hPa, during the Oct-Apr period (Fig. A1; left column), displays significant upper-level structure associated with the MJO. At day-0, upper-level convergence out-flow is noticed with subtropical cyclone flow anomalies over the Indian Ocean warm pool and Pacific anti-cyclonic completing a quadrupole rotational circulation. The presence of extratropical wave trains modulating the dipole SESA-SACZ convective structure is clear when the rotational component of circulation is considered. This modulation is clear during the May-September period in agreement with the results presented in Fig. 7 and Table 1.

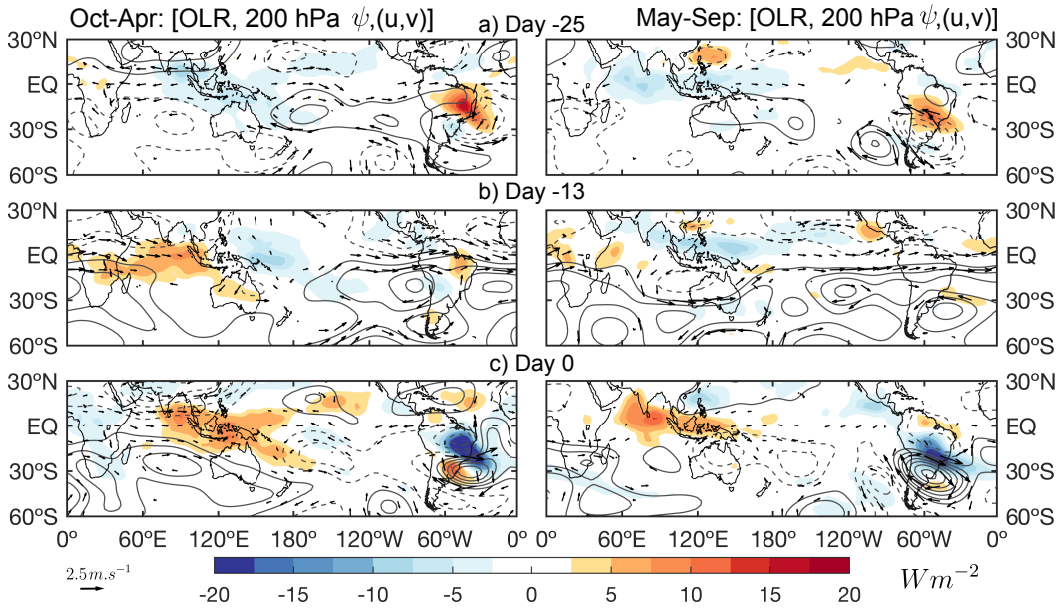


A1. As in Figure 4, but contours represent streamfunction. The streamfunction ($\psi$) contour interval is $1.5\times10^6$ m$^2$ s$^{-1}$.

## Appendix B Upper-level Regression fields

Figure B1 shows the LFI regression patterns of upper-level winds and velocity potential ($\chi$)). It was constructed in order to show the contribution of the IGW modes (Fig. B1b) in the total fields, mainly during the Oct-Apr season. Indeed, it well-described the wavenumber-1 ($k$=1) structure associated with eastward MJO propagation into South America.

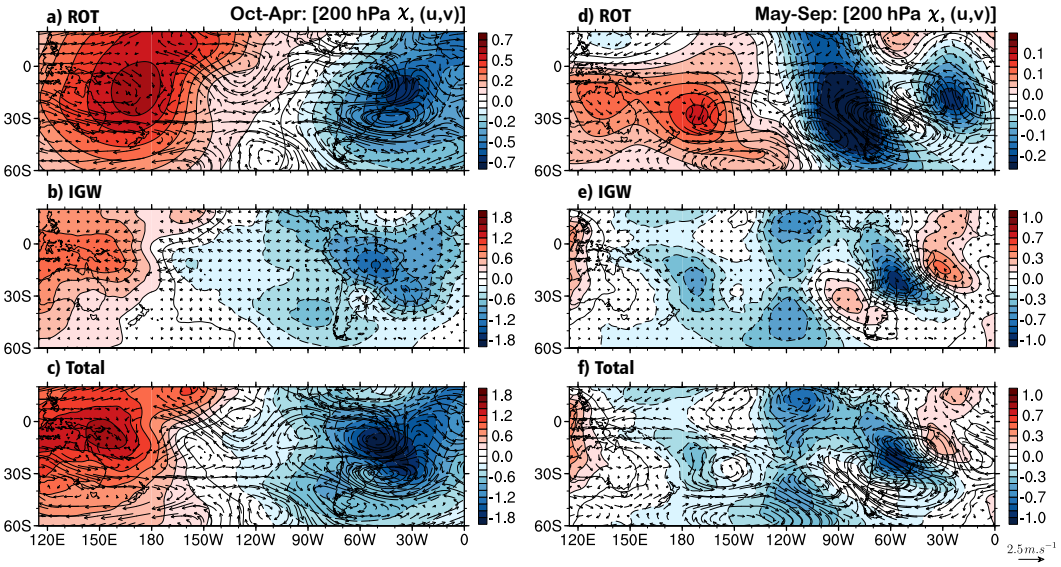


B1. As in Figure 7, but showing upper-level velocity potential ($\chi$) instead of streamfunction.

**Table 1.** Low-frequency Intraseasonal (LFI) seasonal cycle and their associated precursors. Dates of the LFI events at day 0 are determined from PC1 of the EOF analysis. Boldface dates indicate that day 0 is observed as an active phase ($Amplitude = (PC1^2 + PC2^2)^{1/2} \geq 1$) in RMM or/and OMI index. In parenthesis are also presented the precursors associated with each event, where T, E, and OP means that LFI events are preceded by tropical, extratropical (HFI), and other precursors, respectively.

| Seasonal cycle of the Low-frequency Intraseasonal (LFI) events and their associated precursor | | | |
|---|---|---|---|
| Year | *Oct-Apr* | *May − Sep* | Total |
| 1979/80 | **04/07 (T)** | 07/04 (OP) | 2 |
| 1980/81 | **03/19 (T/E)**; **04/28 (T/E)** | 06/11 (E); **08/17 (T)** | 4 |
| 1981/82 | **10/08 (T/E)**; 01/11 (T); 03/09 (T); **04/15 (T)** | 06/22 (T); 08/13 (OP) | 6 |
| 1982/83 | **02/01 (T)**; **03/20 (T/E)** | 05/28 (OP); **09/11 (T)** | 4 |
| 1983/84 | - | 06/14 (OP); | 1 |
| 1984/85 | **10/24 (T)**; 11/30 (OP); **01/20 (T)**; **03/03 (T/E)** | 09/29 (OP) | 5 |
| 1985/86 | 12/02 (T); **12/30 (T/E)** | 05/07 (T/E); **07/12 (T)**; **08/21 (T/E)** | 5 |
| 1986/87 | 10/09 (T/E); **12/25 (E)** | **05/01 (T)** | 3 |
| 1987/88 | 10/02 (OP); 02/14 (T); **04/19 (T)** | - | 3 |
| 1988/89 | 10/08 (T); **04/23 (T)** | **06/17(T)** | 3 |
| 1989/90 | **12/19 (T)**; **02/20 (T)** | **05/09 (T)**; **07/17 (T/E)**; **08/29 (T)** | 5 |
| 1990/91 | **10/24(T)**; **11/30 (T)**; **01/08 (T)**; 03/21 (T) | **05/09 (T)**; **06/17 (T)**; **09/23 (T)** | 7 |
| 1991/92 | **11/11 (T)**; **01/27 (T)**; **04/22 (T)** | **07/04 (T)**; **09/14 (E)** | 5 |
| 1992/93 | **02/18 (T)**; 04/01 (T) | **08/15 (T/E)**; 09/19 (E) | 4 |
| 1993/94 | **12/30 (E)**; **03/07 (T)** | **05/27 (T)**; 09/04 (OP) | 4 |
| 1994/95 | **10/14 (T)**; 11/23 (OP); 02/03 (T) | 05/13 (OP) | 4 |
| 1995/96 | 10/07 (T); **03/11 (T)** | **05/19 (T)**; **06/28 (T)**; 09/05 (T) | 5 |
| 1996/97 | **11/20 (T)** | **06/05 (T/E)**; 08/07 (E); 09/17 (OP) | 4 |
| 1997/98 | **12/04 (OP)**; **01/16 (T/E)** | 08/07 (OP) | 3 |
| 1998/99 | **01/05 (OP)**; **03/04 (T)** | **05/08 (T/E)**; **09/17 (T)** | 4 |
| 1999/00 | 10/26 (T); **12/27 (T/E)**; 02/02 (OP); 04/19 (E) | **09/07 (T)** | 5 |
| 2000/01 | **11/05 (T)**; **12/12 (T/E)** | **05/16 (T)**; **07/22 (T)** | 4 |
| 2001/02 | **10/16 (T)**; **01/06 (T)** | **07/08 (T/E)**; 09/12 (T) | 4 |
| 2002/03 | **11/02 (OP)**; **12/14 (T)** | **06/02 (T)** | 3 |
| 2003/04 | **11/02 (T)**; **01/11 (T/E)** | **07/12 (T)**; **08/19 (T)** | 4 |
| 2004/05 | **10/14 (T/E)**; **04/26 (T/E)** | 06/26 (OP); **09/27 (T)** | 4 |
| 2005/06 | **02/08 (T)** | **05/23 (T/E)** | 2 |
| 2006/07 | 12/07 (OP); **02/12 (T/E)**; 04/20 (T) | **05/24 (T/E)**; **07/23 (T)** | 5 |
| 2007/08 | **12/02 (T/E)**; **01/27 (T)**; **04/05 (T)** | 06/23 (OP); 08/03 (OP); **09/25 (T)** | 6 |
| 2008/09 | 11/20 (OP); **03/31 (T)** | 07/22 (OP) | 3 |
| 2009/10 | **10/27 (T/E)**; **12/25 (T)** | **05/29 (T)**; **07/26 (OP)** | 4 |
| 2010/11 | **03/04 (OP)** | - | 1 |
| 2011/12 | **10/12 (T/E)**; 03/18 (OP) | 07/22 (OP) | 3 |
| 2012/13 | 11/16 (T); **01/22 (T/E)**; 04/17 (T) | 06/19 (E) | 4 |
| 2013/14 | 12/18 (E); **02/23 (E)** | **07/25 (E)**; 09/20 (OP) | 4 |
| 2014/15 | **01/31 (T)**; 04/28 (T) | **07/06 (T/E)**; 08/30 (T) | 4 |
| 2015/16 | **01/14 (T)**; 03/27 (T) | **06/06 (T)**; 08/27 (T) | 4 |